J. Fluid Mech. (2007), *vol.* 587, *pp.* 139–161.
doi:10.1017/S0022112007007124 Printed in the United Kingdom

The intermediate Rossby number range and two-dimensional–three-dimensional transfers in rotating decaying homogeneous turbulence

LYDIA BOUROUIBA[1] AND PETER BARTELLO[1,2]

[1]Department of Atmospheric & Oceanic Sciences, McGill University, Montréal, Québec, Canada

[2]Department of Mathematics & Statistics, McGill University, Montréal, Québec, Canada

(Received 9 March 2006 and in revised form 7 May 2007)

Rotating homogeneous turbulence in a finite domain is studied using numerical simulations, with a particular emphasis on the interactions between the wave and zero-frequency modes. Numerical simulations of decaying homogeneous turbulence subject to a wide range of background rotation rates are presented. The effect of rotation is examined in two finite periodic domains in order to test the effect of the size of the computational domain on the results obtained, thereby testing the accurate sampling of near-resonant interactions. We observe a non-monotonic tendency when Rossby number Ro is varied from large values to the small-Ro limit, which is robust to the change of domain size. Three rotation regimes are identified and discussed: the *large*-, the *intermediate*-, and the *small-Ro* regimes. The intermediate-Ro regime is characterized by a positive transfer of energy from wave modes to vortices. The three-dimensional to two-dimensional transfer reaches an initial maximum for $Ro \approx 0.2$ and it is associated with a maximum skewness of vertical vorticity in favour of positive vortices. This maximum is also reached at $Ro \approx 0.2$. In the intermediate range an overall reduction of vertical energy transfer is observed. Additional characteristic horizontal and vertical scales of this particular rotation regime are presented and discussed.

1. Introduction

Rotating frame effects have a crucial influence on large-scale atmospheric and oceanic flows as well as some astrophysical and engineering flows in bounded domains (turbine rotor, rotating spacecraft reservoirs or Jupiter's atmosphere, for example). The Coriolis force appears only in the linear part of the momentum equations, but if strong enough, it can radically change the nonlinear dynamics. The strength of the applied rotation is only appreciable if it is comparable with the nonlinear term. The Rossby number, $Ro = U/2\Omega L$, is a dimensionless measure of the relative size of these terms. Here, Ω is the background rotation rate and U and L are characteristic length and velocity scales, respectively.

When the Coriolis force is applied, inertial waves are solutions of the linear momentum equations. Their frequencies vary from zero to 2Ω (Greenspan 1968). The zero-linear-frequency modes correspond to two-dimensional structures (e.g. shear layers, vortices, etc.), independent of the direction parallel to the rotation axis.

Unlike the rotating-stratified case, the zero-frequency modes in the rotating problem are not related to a third normal mode of the linear operator. However, it is common to still refer to these modes as vortical modes as discussed below in § 2. In the full

nonlinear problem, the large range of frequencies of the inertial waves is at the origin of a complex nonlinear interplay of interactions involving the two-dimensional structures and the wave modes (e.g. resonant triad interactions, quartets, etc.). The dynamics of the two-dimensional structures are, however, slow compared to the time scale of the three-dimensional flow, if Ro is low. This motivated previous work by Benney & Saffman (1966) and Newell (1969) among others. They employed multiple-time-scale asymptotic techniques in the strong rotation limit. Newell (1969) showed that the exact and near-resonant interactions play an important role on a time scale of $O(1/Ro)$, given that the linear time scale is of $O(Ro)$. In this limit, only the resonant and the near-resonant triads are thought to make a significant contribution on the slow time scale, thereby governing the nature of two-dimensional–three-dimensional interactions in that limit.

In this limit, several modal decompositions can be used. One is the helical mode decomposition employed by Greenspan (1968), Cambon & Jacquin (1989), Waleffe (1993), Smith & Waleffe (1999) and Morinishi, Nakabayashi & Ren (2001). Starting from this or similar decompositions, resonant wave theories have been developed, leading to the derivation of an averaged equation. For example, Babin, Mahalov & Nicolaenko (1998) showed that the Navier–Stokes equations can be decomposed into equations governing a three-dimensional (wave modes) subset, a decoupled two-dimensional subset (the averaged equation), and a component that behaves as a passive scalar. Using the resonant wave theory approach, Waleffe (1993) also argued that nonlinear transfers in rotating turbulence are preferentially towards larger, but non-vortical (i.e. not zero-frequency or two-dimensional), vertical scales in the strong rotation limit.

Several experiments in rotating turbulence have been performed, such as those by McEwan (1969, 1976), Hopfinger, Browand & Gagne (1982), Jacquin *et al.* (1990), Baroud *et al.* (2002) and Morize, Moisy & Rabaud (2005). The experiments showed an increase of the correlation lengths along the axis of rotation. In other words, rapid rotation leads to a tendency for two-dimensionalization of an initially isotropic flow. A predominance of cyclonic over anticyclonic activity and a reduction of energy decay have also been observed for certain rotation rates ($Ro \sim O(1)$).

Various numerical simulations have been performed to examine the problem of rotating turbulence, such as the decaying turbulence simulations of Bardina, Ferziger & Rogallo (1985) and Bartello, Métais & Lesieur (1994). The last was the first to demonstrate numerically the breaking of the vorticity symmetry for Rossby numbers of order one in decaying homogeneous turbulence. Note that this preferential destabilization of anticyclones in rotating flows for a Rossby number of order one had previously been observed in confined and free shear flows (mixing layers and plane wakes). Examples are found in Johnson (1963), Rothe & Johnston (1979), Witt & Joubert (1985), Tritton (1992) and Bidokhti & Tritton (1992). The results above support the idea of the emergence of a strong anisotropy by the alignment of the vorticity vector to the rotation axis and the stability of this configuration. They are *a priori* consistent with the tendency of the flow to two-dimensionalize, except for the symmetry breaking, which is not a property of two-dimensional turbulence.

Many studies of forced rotating homogeneous turbulent flow simulations have been performed, including Yeung & Zhou (1998), Smith & Waleffe (1999) and Chen *et al.* (2005). They observed a strong upscale transfer of energy toward larger vertical scales for low Ro. Unlike the two-dimensional inverse cascade, a k_h^{-3} spectrum was observed in forced simulations by Smith & Waleffe (1999), where k_h is the horizontal wavenumber, Which is smaller than that of the forcing. A similar behaviour occurs

at only the higher of the two Rossby numbers examined in Chen *et al.* (2005). The lower-Ro simulation displayed behaviour consistent with a reduction of the interactions between two-dimensional modes and the rest of the flow. The breaking of the vorticity symmetry, identified in the decay simulations of Bartello *et al.* (1994), also appeared in the forced simulation of Smith & Waleffe (1999). This non-two-dimensional property is not taken into account in current theories involving resonant triads. Smith & Lee (2005) found that near-resonant triads have an important role in the vorticity asymmetry.

The scope of this paper is restricted to flows in bounded domains, with discrete wavenumbers. The numerical studies in finite and infinite domains are both idealizations of the rotating flows found in nature and industry. Both approaches have advantages for and major limitations to direct practical applications. In any case, if, as has been observed, the integral scale along the rotation axis grows, then presumably it will eventually fill a large part of the flow domain. When this occurs further progress in understanding the flow will depend on the precise details of its geometry. It is therefore worth mentioning the numerous studies of the problem in unbounded domains (continuous wavenumbers), even if the real flows of interest in this paper are those found in finite natural or manufactured domains. Such studies include axisymmetric EDQNM developments on the basis of helical modes two-point closure found in Cambon & Jacquin (1989) and Cambon, Mansour & Godeferd (1997). The two-point closure model used in the former showed a positive 'angular energy transfer' toward the zero-frequency spectral plane (i.e. two-dimensional modes), which is consistent with the weak turbulence analysis, performed in Waleffe (1992) and Waleffe (1993). In Cambon *et al.* (1997) numerical simulations of the first-order decoupling at finite Ro are said to be inconclusive. The unrealistic geometry is said to lead to a lack of angular resolution of the discrete set of wave vectors.

Following the standard weak turbulence approach (Benney & Newell 1969), several analytical studies have been performed in which nonlinear interactions govern the long-time behaviour in various flows (e.g. Caillol & Zeitlin 2000 for the internal gravity waves, Galtier *et al.* 2000 for incompressible magnetohydrodynamics, Galtier 2003 and Bellet *et al.* 2006 for the specific case of inertial waves). Cambon, Rubinstein & Godeferd's (2004) extended wave turbulence theory suggested that two-dimensionalization cannot rigorously be reached even for infinite rotation rates in continuous and unbounded domains. They demonstrated the presence of new volume and principal value integrals that maintain the coupling between slow and rapid modes.

Bellet *et al.* (2006) aimed to capture the dynamics for asymptotically high rotation rates, for which resonant interactions are predicted by wave–turbulence theories to have a dominant contribution to the dynamics. An asymptotic quasi-normal Markovian (AQNM) model was developed by the authors, investigating the dynamics of only the resonant inertial wave interactions between three-dimensional modes. In fact, the AQNM model cannot capture the resonant triads involving zero-frequency (two-dimensional) modes. An angular energy spectrum is obtained numerically and it is found that the energy density is large near the perpendicular wave vector plane. The singularity is found to be integrable as in other wave–turbulence results such as Galtier (2003). AQNM is discussed further in § 2.

The remainder of the paper in presented as follows. In § 2 the governing equations, the normal mode decomposition and wave theory are reviewed and the modal decomposition is introduced. The numerical methodologies are presented in more detail in § 3. In § 4, three rotation regimes are identified, showing a non-monotonic

tendency of the dynamics and vorticity asymmetry as Ro decreases. A general dynamical picture of decaying turbulent flows for moderate to small Ro in bounded domains is discussed and summarized. Conclusions are given in § 5.

2. Equations and rotating turbulence theories

In a rotating frame of reference, the incompressible momentum equations are

$$\frac{\partial \boldsymbol{u}}{\partial t} + (\boldsymbol{u}\cdot\nabla)\boldsymbol{u} + 2\Omega\hat{\boldsymbol{z}}\times\boldsymbol{u} = -\nabla\tilde{p} + \boldsymbol{d}_p(\boldsymbol{u}), \qquad \nabla\cdot\boldsymbol{u} = 0, \tag{2.1}$$

where $\Omega = \Omega\hat{\boldsymbol{z}}$ is the rotation vector, the velocity is $\boldsymbol{u} = (u, v, w)$ and $\tilde{p}$ includes the pressure term of the inertial frame, the centrifugal term and other contributions from conservative forces. The usual viscous term corresponds to $p = 1$ in the hyperviscosity $\boldsymbol{d}_p(\boldsymbol{u}) = (-1)^{p+1}\nu_p(-\nabla^2)^p\ \boldsymbol{u}$. Without loss of generality, the rotation axis has been chosen to be the vertical. For the non-dimensionalization we use $(2\Omega)^{-1}$, L and U as characteristic time, length and velocity, respectively. The non-dimensional equations become

$$\frac{\partial \boldsymbol{u}}{\partial t} + Ro\ (\boldsymbol{u}\cdot\nabla)\boldsymbol{u} + \hat{\boldsymbol{z}}\times\boldsymbol{u} = -\nabla p + \boldsymbol{D}_p(\boldsymbol{u}), \qquad \nabla\cdot\boldsymbol{u} = 0, \tag{2.2}$$

where Ro is the Rossby number. As $Ro \to 0$, (2.2) evolves on both a slow vortical time scale $\tau_1 = Ro\ t$ and a fast wave time scale $\tau_0 = t$, where t is the non-dimensional time. A two-time-scale asymptotic expansion can be performed. The leading-order contribution has inertial wave solutions of non-dimensional frequencies $\omega_{s_k}(\boldsymbol{k}) = s_k\hat{\boldsymbol{z}}\cdot\boldsymbol{k}/|\boldsymbol{k}| = s_k k_z/k = s_k\cos(\theta_k)$, where $s_k = \pm 1$ and θ_k is the angle between the axis of rotation (here $\hat{\boldsymbol{z}}$) and the Fourier-space wavevector $\boldsymbol{k}$. In the following $\omega_{s_k}(\boldsymbol{k})$ is also referred to as ω_{s_k}. The associated normal modes, also called *helical modes* (Waleffe 1993), are

$$\boldsymbol{N}^{s_k} = \left(\frac{\hat{\boldsymbol{z}}\times\boldsymbol{k}}{|\hat{\boldsymbol{z}}\times\boldsymbol{k}|}\times\frac{\boldsymbol{k}}{|\boldsymbol{k}|} + \mathrm{i}s_k\frac{\hat{\boldsymbol{z}}\times\boldsymbol{k}}{|\hat{\boldsymbol{z}}\times\boldsymbol{k}|}\right), \tag{2.3}$$

where $\mathrm{i}^2 = -1$ and $\boldsymbol{N}^{s_k}(\boldsymbol{k})$ are the eigenmodes of the curl operator obtained by solving

$$\mathrm{i}\boldsymbol{k}\times\boldsymbol{n}(\boldsymbol{k}) = \lambda\boldsymbol{n}(\boldsymbol{k}). \tag{2.4}$$

The solutions for λ are $+|\boldsymbol{k}|$ and $-|\boldsymbol{k}|$, which give the eigenvectors $\boldsymbol{N}^+$ and $\boldsymbol{N}^-$ for $\boldsymbol{n}$. Using these solutions in (2.2) gives us the expression for the eigenmodes associated with the linear rotation operator. They are called inertial waves (Greenspan 1968) and are given by

$$\boldsymbol{N}^{s_k}(\boldsymbol{k})\exp(\mathrm{i}\omega_{s_k}(\boldsymbol{k})t), \tag{2.5}$$

where $\boldsymbol{N}^+(\boldsymbol{k})$ is the complex conjugate of $\boldsymbol{N}^-(\boldsymbol{k})$ (e.g. Cambon & Jacquin 1989; Waleffe 1992, 1993). The velocity field in Fourier-space can therefore be written

$$\boldsymbol{u}(\boldsymbol{k}, \tau_0, \tau_1) = \sum_{s_k=\pm} A_{s_k}(\boldsymbol{k}, \tau_1)\ \boldsymbol{N}^{s_k}(\boldsymbol{k})\exp\left(\mathrm{i}\omega_{s_k}\tau_0\right). \tag{2.6}$$

Note that even if a time-scale separation analysis is used here ($\partial_t \to \partial_{\tau_0} + Ro\partial_{\tau_1}$), low-frequency waves are still present in the system. The analysis gives an equation for the slow evolution of the amplitudes A_{s_k}:

$$\partial_{\tau_1} A_{s_k}(\boldsymbol{k}, \tau_1) = -\frac{1}{4}\sum_{\substack{k=p+q \\ s_p, s_q}}^{\omega_{s_k}+\omega_{s_p}+\omega_{s_q}=0} C_{\boldsymbol{kpq}}^{s_k s_p s_q} A_{s_p}(\boldsymbol{p}, \tau_1)\ A_{s_q}(\boldsymbol{q}, \tau_1). \tag{2.7}$$

$C_{\boldsymbol{kpq}}^{s_k s_p s_q}$ are the interaction coefficients shown by Waleffe (1992) to have the form

$$C_{\boldsymbol{kpq}}^{s_k s_p s_q} = (s_p p - s_q q)\,(\boldsymbol{N}^{s_p} \times \boldsymbol{N}^{s_q}) \cdot \boldsymbol{N}^{*\,s_k}, \tag{2.8}$$

where the star stands for the complex conjugate. The only interacting triads that have a significant contribution on the slow time scale τ_1 in (2.7) are those that satisfy the *resonance condition*

$$\omega_{s_k}(\boldsymbol{k}) + \omega_{s_p}(\boldsymbol{p}) + \omega_{s_q}(\boldsymbol{q}) = 0. \tag{2.9}$$

In other words, those satisfying

$$\boldsymbol{k} = \boldsymbol{p} + \boldsymbol{q} \quad \text{and} \quad s_k \frac{\boldsymbol{k}_z}{|\boldsymbol{k}|} = s_p \frac{\boldsymbol{p}_z}{|\boldsymbol{p}|} + s_q \frac{\boldsymbol{q}_z}{|\boldsymbol{q}|}. \tag{2.10}$$

The frequencies of the inertial waves vary from 0 to 2Ω. The zero-frequency modes belong to the two-dimensional Fourier-space plane defined by $k_z = 0$, corresponding to the vertically averaged real-space velocity field. In the rotating-stratified case, the linear operator has two inertia–gravity wave eigenmodes and a third distinct vortical quasi-geostrophic normal mode with zero frequency. Unlike that case, the zero-frequency mode of the present problem with rotation only is not a third normal mode of the linear operator. It is only derived from the wave modes for the particular value of $k_z = 0$. In that sense, it is analogous to the stratified shear modes, found on the one-dimensional k_z-axis in Fourier-space. In the problem with rotation alone, however, the zero-frequency modes describe a two-dimensional Fourier-space plane (defined by $k_z = 0$). As these modes form the slowly varying components of the flow, we refer to them as vortical. We introduce the following notation:†

$$\left.\begin{array}{l} \text{if } \boldsymbol{k} \in V_{\boldsymbol{k}} = \{\boldsymbol{k} | k \neq 0 \text{ and } k_z = 0\} \text{ then } \boldsymbol{u}(\boldsymbol{k}) = \boldsymbol{u}_{2D}(\boldsymbol{k}_h) + w(\boldsymbol{k}_h)\,\hat{\boldsymbol{z}}, \\ \text{if } \boldsymbol{k} \in W_{\boldsymbol{k}} = \{\boldsymbol{k} | k \neq 0 \text{ and } k_z \neq 0\} \text{ then } \boldsymbol{u}(\boldsymbol{k}) = \boldsymbol{u}_{3D}(\boldsymbol{k}). \end{array}\right\} \tag{2.11}$$

We can also decompose the total energy $E = \frac{1}{2}\sum_{\boldsymbol{k}} |\boldsymbol{u}(\boldsymbol{k})|^2$ into three contributions‡

$$E = E_{2D} + E_w + E_{3D}, \tag{2.12}$$

with

$$E_{2D} = \frac{1}{2}\sum_{\boldsymbol{k} \in V_{\boldsymbol{k}}} |\boldsymbol{u}_{2D}(\boldsymbol{k})|^2, \quad E_w = \frac{1}{2}\sum_{\boldsymbol{k} \in V_{\boldsymbol{k}}} |w(\boldsymbol{k})|^2 \qquad E_{3D} = \frac{1}{2}\sum_{\boldsymbol{k} \in W_{\boldsymbol{k}}} |\boldsymbol{u}(\boldsymbol{k})|^2, \tag{2.13}$$

along with their corresponding spectra. The latter are governed by

$$\left.\begin{array}{l} \dfrac{\partial E_{3D}}{\partial t}(\boldsymbol{k} \in W_{\boldsymbol{k}}, t) = (T_{3-33} + T_{3-32} + T_{3-3w})(\boldsymbol{k} \in W_{\boldsymbol{k}}, t) - \tilde{D}_{p,3D}(\boldsymbol{k} \in W_{\boldsymbol{k}}, t), \\ \dfrac{\partial E_{2D}}{\partial t}(\boldsymbol{k} \in V_{\boldsymbol{k}}, t) = (T_{2-22} + T_{2-33})(\boldsymbol{k} \in V_{\boldsymbol{k}}, t) - \tilde{D}_{p,2D}(\boldsymbol{k} \in V_{\boldsymbol{k}}, t), \\ \dfrac{\partial E_w}{\partial t}(\boldsymbol{k} \in V_{\boldsymbol{k}}, t) = (T_{w-2w} + T_{w-33})(\boldsymbol{k} \in V_{\boldsymbol{k}}, t) - \tilde{D}_{p,w}(\boldsymbol{k} \in V_{\boldsymbol{k}}, t) \end{array}\right\} \tag{2.14}$$

with T being the Fourier-space energy transfer and $\tilde{D}_{p,2D \text{ or } 3D \text{ or } w}$ the two-dimensional, three-dimensional or vertically averaged w spectral dissipation terms, respectively. Transfers are distinguished by the types of interactions, e.g. 2-33 stands for the interactions between two three-dimensional wave modes that contribute to

† An analogous semi-axisymmetric decomposition was introduced by Cambon & Jacquin (1989) in terms of energy, polarization and helicity, denoted $e(k, \cos\theta)$, $Z(k, \cos\theta)$ and $h(k, \cos\theta)$, respectively.

‡ E_{3D}, E_{2D} and E_w correspond to $e(k, \cos\theta \neq 0)$, $(e - Z)|_{\cos\theta = 0}$ and $(e + Z)|_{\cos\theta = 0}$, respectively.

the two-dimensional equation. Note that the $T_{i\text{-}jk}$ terms are symmetric in j and k. Only a subset of three-dimensional wavenumbers can satisfy the resonance condition in the 3-33, 3-32 and 3-3w interactions, but from (2.8) it follows that 3-32 and 3-3w resonant triads do not transfer energy to the two-dimensional and w modes, respectively (Waleffe 1993). They are therefore said to be 'catalytic' for interactions between the two wave modes of the same frequency. This last property is a key point in asymptotic decoupling theories. In the $Ro \to 0$ limit, it is thought that only resonant interactions make a significant contribution to the slow dynamics. Therefore, the asymptotic energy equations in this limit are

$$\left.\begin{aligned} \frac{\partial E_{3D}}{\partial t}(\boldsymbol{k} \in W_{\boldsymbol{k}}, t) &= T_{3\_33,res} + T_{3\_32,res} + T_{3\_3w,res} - \tilde{D}_{p,3D}, \\ \frac{\partial E_{2D}}{\partial t}(\boldsymbol{k} \in V_{\boldsymbol{k}}, t) &= T_{2\_22} - \tilde{D}_{p,2D}, \\ \frac{\partial E_{w}}{\partial t}(\boldsymbol{k} \in V_{\boldsymbol{k}}, t) &= T_{w\_2w} - \tilde{D}_{p,w}, \end{aligned}\right\} \tag{2.15}$$

where the subscript $\{i\text{-}jk, res\}$ stands for resonant $i\text{-}jk$ interactions (2.10). The time and wavenumber dependence in (2.15) has been omitted. The 2-22 and w-2w interactions are trivially resonant, since all modes involved have zero frequency. It appears from (2.15) that the equation for E_{2D} is decoupled from the E_{3D} equation and is also identical to that governing two-dimensional turbulence. The equation for E_w is also decoupled from that of E_{3D} and takes the form of that of a passive tracer advected by the two-dimensional velocity field $\boldsymbol{u}_{2D}$. On the other hand, the E_{3D} equation is not decoupled since the three-dimensional energy interactions remain affected by the $k_z = 0$ dynamics through the set of catalytic resonant triads 3-32 and 3-3w.

Waleffe (1993) and Cambon *et al.*(1997) found that the 3-33 resonant subset plays an important role in the quasi-two-dimensionalization of the flow. According to their argument, these interactions transfer the E_{3D} energy preferentially in an angular sense to close to, but not exactly, zero-frequency waves. Based on the greater complexity of the resonant subset of 3-33 interactions compared to that of 3-23, it has been argued by Babin, Mahalov & Nicolaenko (1996, 1998) that flow in the $Ro \to 0$ limit would display not only the E_{2D} decoupled dynamics, but an infinity of approximate adiabatic invariants corresponding to a decoupling of each constant k_z Fourier-space surface. Such a result implies a freezing of vertical transfer in the strong-rotation limit.

In Bellet *et al.* (2006), the AQNM model is intended to specifically capture only the resonant interactions and thus only the asymptotic regime. The equations used in AQNM are those of an unbounded domain in real space, corresponding to a continuous distribution of wavevectors in Fourier-space. A correspondence with the equations presented here is nevertheless perhaps possible. In fact, in Bellet *et al.* (2006) the resonance condition is not applicable in the vicinity of the $k_z = 0$ Fourier-plane. Two-dimensional and w modes introduced in (2.11) are therefore excluded from the AQNM model. Thus, AQNM is equivalent to a modified (2.15), in which only the three-dimensional modes are retained, i.e equivalent to

$$\frac{\partial E_{3D}}{\partial t}(\boldsymbol{k} \in W_{\boldsymbol{k}}, t) = T_{3\_33,res}(\boldsymbol{k} \in W_{\boldsymbol{k}}, t), \tag{2.16}$$

where both $T_{3-32,res}$ and $T_{3-3w,res}$ terms are removed and the viscosity term is omitted for brevity. Given that the aim of this paper is to focus on two-dimensional–three-dimensional interactions at finite Rossby number and that there are no strictly

resonant interactions capable of such transfer, we necessarily restrict ourselves to a regime where non-resonant interactions are still present. In addition, given that the redistribution of wave energy via the catalytic two-dimensional–three-dimensional resonant-interaction term in the E_{3D} equation is also of interest, we are forced to conclude that there is limited scope in comparing our results with AQNM-type studies.

3. Numerical method and Rossby number

Equations (2.2) are solved numerically using a direct (de-aliased) pseudo-spectral method. The integration domain is triply periodic of length 2π. We use leapfrog time differencing and the Asselin–Robert filter in order to control the computational mode (e.g. Asselin 1972). The filter factor was set to be 10^{-3}. Owing to the anisotropy of the problem we used cylindrical truncation for all our simulations, i.e. k_h, $|k_z| < k_t = N/3$, where N^3 is the number of spatial collocation points (referred to as resolution) and $k_h = \sqrt{k_x^2 + k_y^2}$ is the horizontal wavenumber. The 'two-thirds rule' was chosen in order to filter the aliasing of the misrepresented wavenumbers introduced by the computation of the nonlinear terms (Boyd 1989). We used a hypervisosity $\boldsymbol{D}_p(\boldsymbol{u})$ in (2.2), with $p = 4$ in order to obtain higher effective Reynolds numbers (e.g. Bartello *et al.* 1994).

Our strategy has been to decompose the fields into waves ($k_z \neq 0$), two-dimensional and w components as in (2.11) and (2.14).

The Rossby number is the dimensionless measure of the relative size of the rotation and the advection terms. It can be defined as $Ro = U/2\Omega L$, where U and L are characteristic length and velocity scales, respectively. Jacquin *et al.* (1990) gave experimental evidence of two relevant Rossby numbers: a *macro*-Rossby number, Ro_{macro}, based on a large length scale (e.g. an integral length scale L) and a *micro*-Rossby, R_{micro}, based on a smaller length scale (a Taylor microscale λ). They observed two distinct and successive transitions at $Ro_{macro} \approx 1$ and $Ro_{micro} \approx 1$. In the reminder of this paper, the following definition of Ro is used:

$$Ro_m = \sqrt{[\omega_z^2]}/(2\Omega), \tag{3.1}$$

with [.] the spatial average and ω_z the vertical vorticity component. Because of the use of the vorticity in (3.1), this definition would correspond to the *micro*-Rossby number in Jacquin *et al.* (1990) and Cambon *et al.* (1997) for close-to-isotropy three-dimensional flows. For this latter flow configuration another definition, $Ro_M = U/2\Omega L$, with L based on the energy-containing large scales, would also be relevant. Ro_M would correspond to the Ro_{macro} in Jacquin *et al.* (1990). For comparison, we computed both Ro_M and Ro_m. Both values are displayed in table 1, thereby testing the sensitivity of the results to the use of either definition. Unless noted otherwise (3.1) is used to compute the Rossby number and it is denoted Ro in the remainder of the paper.

4. Decaying rotating turbulence simulations

4.1. *Non-monotonic tendency as $Ro \to 0$ and its robustness to the change of the size of the domain*

A set of simulations were initialized with fully developed isotropic decaying turbulent fields generated in domains of different sizes. Different rotation rates were then imposed on the resulting fields (table 1).

Ro	Ro_{MS}	Ro_{ML}	Δt_{100}	Δt_{200}	Ro	Ro_{MS}	Ro_{ML}	Δt_{100}	Δt_{200}
0.01	0.008	0.008	5.6×10^{-4}	8.55×10^{-5}	0.172	0.14	0.14	d_1	d_2
0.015	0.012	0.012	8.4×10^{-4}	1.28×10^{-4}	0.189	0.16	0.15	d_1	d_2
0.022	0.018	0.018	1.26×10^{-3}	1.92×10^{-4}	0.20	0.17	0.16	d_1	d_2
0.034	0.028	0.0275	1.9×10^{-3}	2.91×10^{-4}	0.23	0.19	0.191	d_1	d_2
0.05	0.042	0.04	2.8×10^{-3}	4.28×10^{-4}	0.28	0.24	0.23	d_1	d_2
0.060	0.05	0.049	3.39×10^{-3}	5.18×10^{-4}	0.3	0.25	0.25	d_1	d_2
0.066	0.056	0.054	3.7×10^{-3}	5.65×10^{-4}	0.47	0.41	0.4	d_1	d_2
0.073	0.061	0.059	4.1×10^{-3}	6.25×10^{-4}	0.6	0.52	0.5	d_1	d_2
0.08	0.067	0.065	4.5×10^{-3}	6.84×10^{-4}	0.75	0.65	0.63	d_1	d_2
0.088	0.074	0.072	4.94×10^{-3}	7.53×10^{-4}	0.95	0.82	0.8	d_1	d_2
0.097	0.082	0.079	5.44×10^{-3}	8.29×10^{-4}	1.2	1	1.01	d_1	d_2
0.107	0.091	0.088	d_1	9.15×10^{-4}	1.5	1.29	1.26	d_1	d_2
0.117	0.1	0.096	d_1	9.85×10^{-4}	3	2.59	2.5	d_1	d_2
0.13	0.11	0.11	d_1	d_2	10	8.7	8.4	d_1	d_2
0.142	0.12	0.12	d_1	d_2	100	86.3	84.2	d_1	d_2
0.156	0.13	0.13	d_1	d_2	∞	∞	∞	d_1	d_2

TABLE 1. Time steps for the simulations in domains L and S, for each initial Ro, with $d_1 = 5.84 \times 10^{-3}$ and $d_2 = 9.87 \times 10^{-4}$. The *micro*-Rossby number is referred to as Ro. The *macro*-Rossby numbers are denoted Ro_{MS} and Ro_{ML} for the S and L domains, respectively. We introduce rotation on fully developed turbulence with total energies $E_S = 0.234$ and $E_L = 2.254$. Hyperviscosity coefficients are $\nu_{4,S} = 2.602 \times 10^{-11}$ and $\nu_{4,L} = 2.927 \times 10^{-13}$. The initial eddy turnover time scales were $\tau_S = 0.1038$ and $\tau_L = 0.01189$.

We choose to present results of the simulations obtained from grids of resolutions 100^3 and 200^3. For the small-domain simulation (S) (resolution 100^3) the preliminary non-rotating simulation is initialized with an isotropic Gaussian spectrum centred around $k_{i,S} = 6.4$, with width $\sigma_S = 1.6$ and total energy $E_S = 0.41$. The truncation wavenumber is $k_{t,S} = 32$. The set-up for the large domain (resolution 200^3) (L) (twice as as large as S) leads to $k_{t,L} = 66$ and a rescaled spectrum using a stretching coefficient of $\gamma = k_{t,L}/k_{t,S}$ giving $k_{i,L} = 13.2$, $\sigma_L = 3.3$ and $E_L = 3.59$. Initial non-rotating spectra of total energy E are displayed for both simulations in figure 1(*a*).

We chose the two domains and rescaling described above in order to study the sensitivity of the results to a change in the size of the computational domain, rather than a change of resolution (implemented by both a change of resolution and a rescaling argument of the initial fields). This also indirectly allows us to check both the influence of the angular resolution of the discrete domain, and the adequacy of sampling of near-resonant interactions that are linked to the size of the domain.

These preliminary non-rotating simulations were run until the enstrophy maximum was reached (after about 10 large-scale turnover times). The non-rotating fully developed turbulent energy spectra obtained at the end of the preliminary runs are compared in figure 1(*b*). The collapse outside the dissipation range is still good. A horizontal (x, y) slice of the vertical vorticity field ω_z in the large computational domain is displayed in figure 2.

At this point, different rotation rates are applied to the isotropic fully developed turbulence. Parameters such as initial energies, hyperviscosity coefficients and eddy turnover time scales at the end of the preliminary non-rotating simulation are given in table 1. High rotation rates require very long calculations due to time-step limitations imposed by the explicit treatment of the Coriolis term. The initial Ro and associated

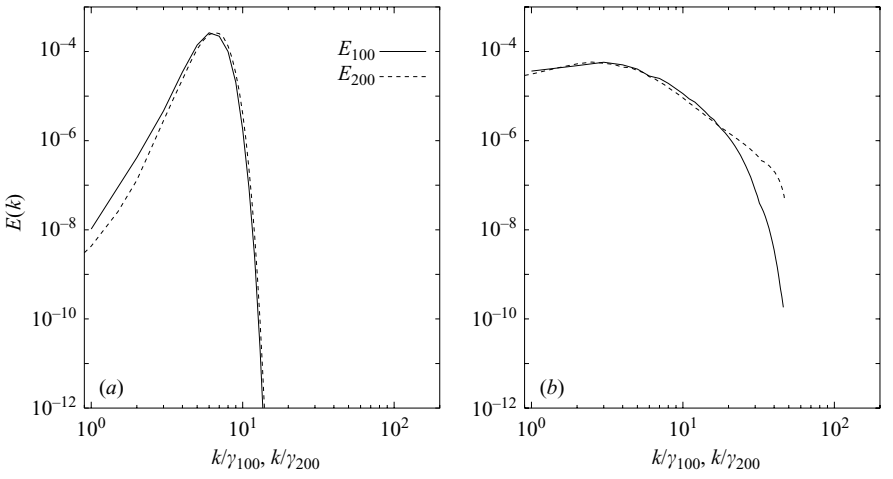

FIGURE 1. Total energy spectra for preliminary non-rotating simulations. (*a*) Spectra of E_S and E_L used to initiate the preliminary run and (*b*) corresponding final spectra of the flow used to initiate the rotating simulations. We present results of the large and small boxes, with $\gamma_S = 1$ and $\gamma_L = 2.062$.

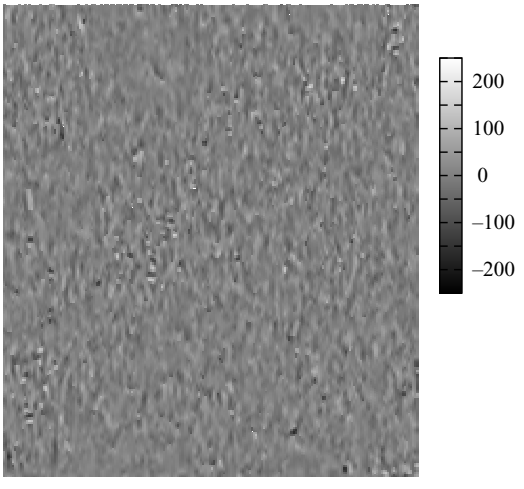

FIGURE 2. Horizontal slice (x, y) of the vorticity field $\boldsymbol{\omega}_z$ at the end of the isotropic simulation. The field is used to initialize the subsequent rotating simulations of the large computational domain.

time steps are also given in table 1. The equivalent large-scale-based Ro_M for each of the simulations in domains L and S is given in table 1.

Figure 3 displays the normalized energy time series of two-dimensional and three-dimensional modes as a function of non-dimensional time for the large-box runs. The curves for the small box are similar and are therefore not shown here. Time has been non-dimensionalized using the initial eddy turnover time scales (table 1). The preliminary non-rotating run shows little vortical energy compared to wave energy, as expected for an isotropic system where the decomposition has no meaning. At the end of this preliminary run, different rotation rates were applied (table 1). We observe three types of behaviour. First, *large-Ro* simulations display a time evolution similar

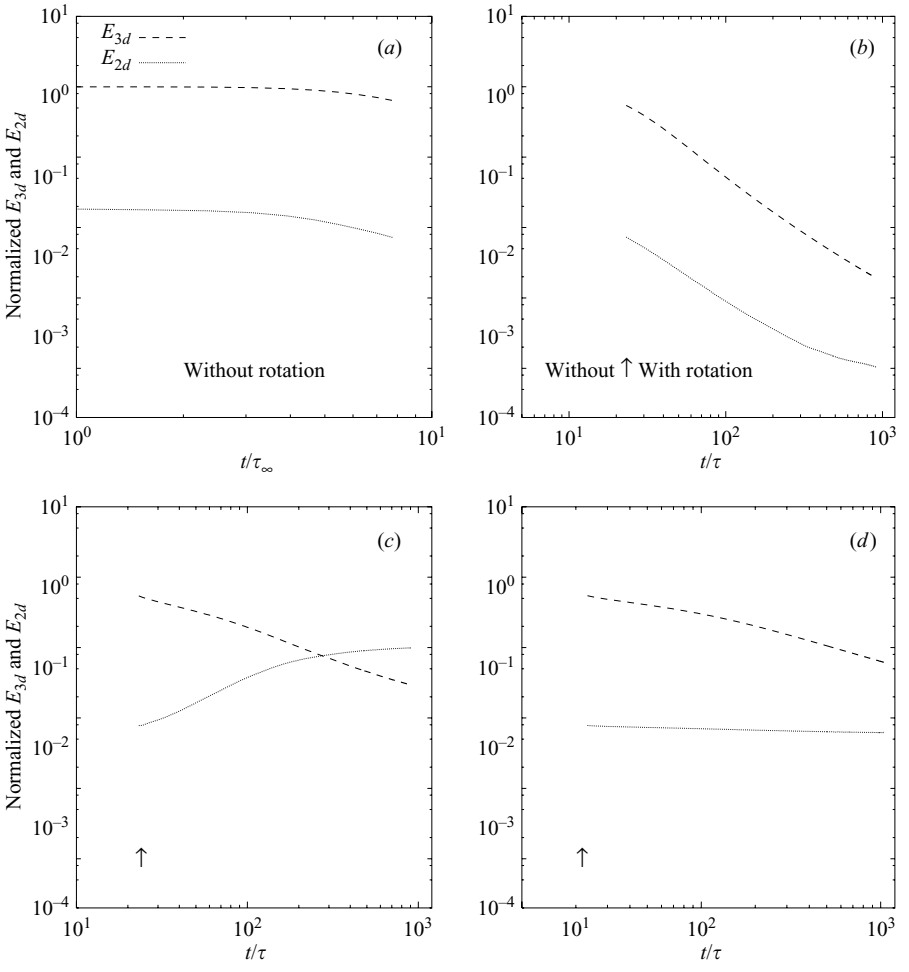

FIGURE 3. Time series of normalized E_{2D} and E_{3D} as a function of the non-dimensional time t/τ, where the eddy turnover time scale for the initial non-rotating run is $\tau_\infty = 0.032$ and the initial eddy turnover time scale for the rotating runs is $\tau = 0.012$. (*a*) The initial non-rotating run, (*b*) $Ro = 100$, (*c*) $Ro = 0.2$ and (*d*) $Ro = 0.01$. All these results were obtained with the large computational box size.

to that of isotropic simulations, where both two-dimensional and three-dimensional energies have the same decay rate (e.g. $Ro = 100$). As rotation increases, we observe a transition to a second regime of slow total energy decay. We call this regime the *intermediate-Ro* range or regime. It is characterized by a growth of E_{2D} with time, while the wave energy decay is reduced. The E_{2D} growth rate reaches a maximum for $Ro \approx 0.2$. We therefore chose to display this particular Ro as an example. Throughout this paper, our discussion of the $Ro \approx 0.2$ simulation applies qualitatively to all intermediate-Ro range simulations. Around $t/\tau \approx 300$ vortical and wave energy curves cross in figure 3(*c*). After that time, most of the energy is two-dimensional. This increase of two-dimensional energy implies a transfer from three-dimensional modes. This is an important characteristic of the intermediate-Ro range. Finally, more rapidly rotating simulations do not display this wave–vortex energy transfer. In fact, the time series show an expected slower decay rate of wave energy, E_{3D}, at $Ro = 0.01$,

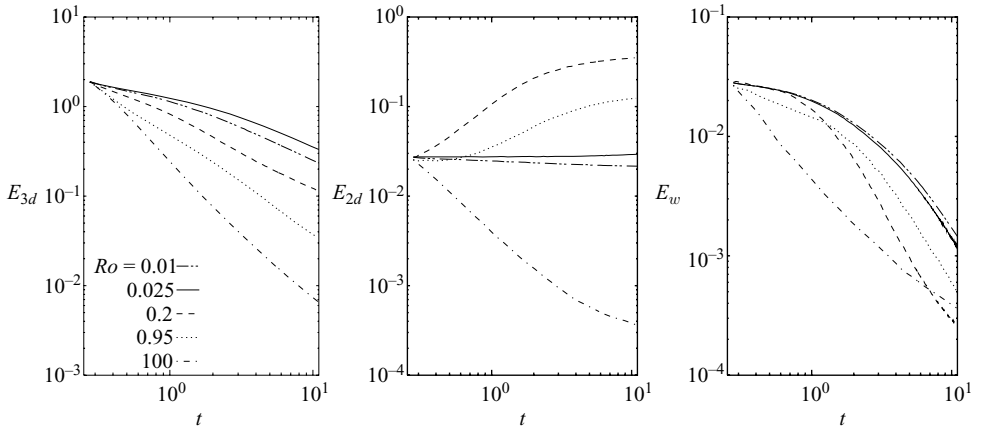

FIGURE 4. Time series for the large-box simulations of the wave energy (*a*), the vortical energy (*b*) and the volume mean square of w, E_w (*c*) (2.14) for $Ro = 100$, 0.95, 0.2, 0.025 and 0.01. Qualitatively similar results were obtained for the small box.

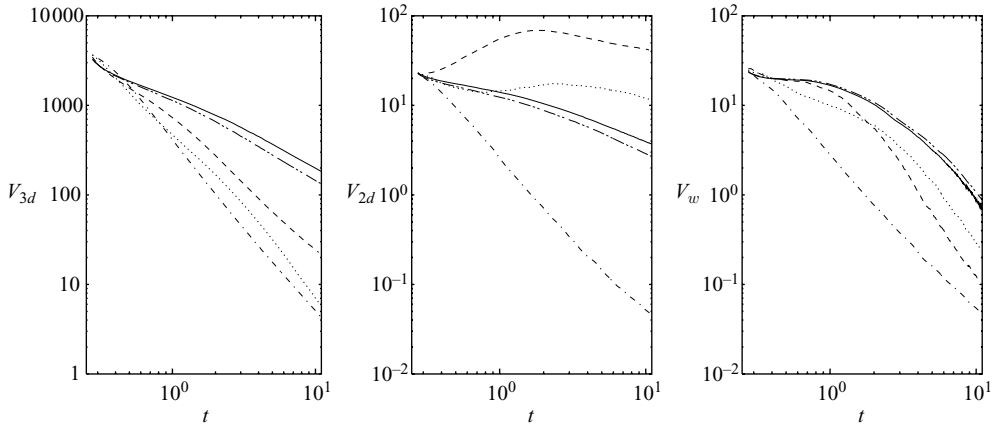

FIGURE 5. Time series for the large-box simulations of the total three-dimensional enstrophy V (*a*), the two-dimensional enstrophy V_{2D} (*b*) and V_w (*c*), for $Ro = 100$, 0.95, 0.2, 0.025 and 0.01 (line styles as in figure 4). Similar results were obtained for the small box.

but only a slight dissipation of E_{2D}, consistent with a negligible transfer between $V_{\boldsymbol{k}}$ and $W_{\boldsymbol{p}}$ modes. Recall that energy does not decay in two-dimensional turbulence in the limit $Re \to \infty$. We refer to this third Ro range as the *small-Ro* regime. Its characteristic is the apparent decoupling of wave and vortex modes that seems to be in agreement with the first-order resonant theories introduced in § 2.

We observe an overall reduction of both total energy and enstrophy decay with rotation. This is consistent with the expected reduction of the energy cascade in rotating turbulence due to phase scrambling. Thus, high values of enstrophy and energy are observed for a longer period of time as Ro decreases. We have already observed that a range of rotation rates, referred to as the *intermediate* range, is characterized by an increase of vortical energy and therefore a strong interaction between wave and vortical modes. Both enstrophy and energy are decomposed following (2.11). We display the resulting time series in figures 4 and 5.

Figure 4 displays the large-box time series of E_{3D}, E_{2D} and E_w. Figure 5 displays the large-domain-size time series of three-dimensional enstrophy given by

$$V_{3D} = \frac{1}{2} \sum_{\boldsymbol{k} \in W_{\boldsymbol{k}}} |\boldsymbol{\omega}(\boldsymbol{k})|^2, \tag{4.1}$$

w enstrophy V_w given by

$$V_w = \frac{1}{2} \sum_{\boldsymbol{k} \in V_{\boldsymbol{k}}} |\boldsymbol{\omega}_h(\boldsymbol{k})|^2, \tag{4.2}$$

and the two-dimensional enstrophy V_{2D} given by

$$V_{2D} = \frac{1}{2} \sum_{\boldsymbol{k} \in V_{\boldsymbol{k}}} |\boldsymbol{\omega}_z(\boldsymbol{k})|^2. \tag{4.3}$$

In these equations $\boldsymbol{\omega}$ is the total vorticity field, $\boldsymbol{\omega}_h = \omega_x \boldsymbol{x} + \omega_y \boldsymbol{y}$ is its horizontal component and $\boldsymbol{\omega}_z$ its vertical component.

Outside the intermediate-Ro range the total energy is dominated by wave energy, E_{3D}. The intermediate-Ro simulations show an increase of E_{2D} with time. The maximum growth rate is reached for $Ro \approx 0.2$ (figure 4). Meanwhile, the enstrophy V_{2D} shows a maximum growth for the same Ro (figure 5). For all Ro E_w decreases with time, i.e. the transfer of energy from modes in $W_{\boldsymbol{k}}$ to modes in $V_{\boldsymbol{k}}$ does not extend to the w mode in the intermediate range. We note from the $Ro = 0.2$ curves in figures 4 and 5 that the rate of decay of E_w and V_w increases when E_{2D} and V_{2D} are large. In fact, if we exclude $Ro = 100$ from this analysis, the $Ro = 0.2$ decay rate of E_w and V_w is the highest in the intermediate- and small-Ro ranges. This is in agreement with the asymptotic equation (2.15) governing E_w, i.e. a decaying passive scalar advected by the two-dimensional flow. On the other hand, the intermediate-Ro range is obviously not described by the decoupled equations (2.15), and so no further comparisons can be made. Concerning the small-Ro range, $E_{2D} \approx \text{const}$ and $V_{2D} \sim t^{-0.625}$. With all necessary caution, it is interesting to note that this decay rate is consistent with recent observed decaying two-dimensional turbulence results.

In order to solidify the observed separation of regimes with Ro and the non-monotonic tendency to reach the $Ro \to 0$ limit, we consider the integrated energy transfer between one mode in $V_{\boldsymbol{k}}$ and two modes in $W_{\boldsymbol{k}}$. The integration of (2.14) over wavevectors gives

$$\left.\begin{aligned} \frac{\partial E_{3D}}{\partial t} &= -(\mathscr{T}_{23} + \mathscr{T}_{w3}) - \tilde{D}_{p,3D}, \\ \partial \frac{E_{2D}}{\partial t} &= \mathscr{T}_{23} - \tilde{D}_{p,2D}, \\ \frac{\partial E_w}{\partial t} &= \mathscr{T}_{w3} - \tilde{D}_{p,w}, \end{aligned}\right\} \tag{4.4}$$

where

$$\left.\begin{aligned} \mathscr{T}_{23}(t; Ro) &= \int T_{2\_33}(\boldsymbol{k} \in V_{\boldsymbol{k}}, t; Ro)\ \mathrm{d}^3\boldsymbol{k} \ = -\int T_{3\_23}(\boldsymbol{k} \in W_{\boldsymbol{k}}, t; Ro)\ \mathrm{d}^3\boldsymbol{k}, \\ \mathscr{T}_{w3}(t; Ro) &= \int T_{w\_33}(\boldsymbol{k} \in V_{\boldsymbol{k}}, t; Ro)\ \mathrm{d}^3\boldsymbol{k} = -\int T_{3\_3w}(\boldsymbol{k} \in W_{\boldsymbol{k}}, t; Ro)\ \mathrm{d}^3\boldsymbol{k}. \end{aligned}\right\} \tag{4.5}$$

Because of high-frequency waves in rapidly rotating simulations, rapidly fluctuating time series of the integrated energy transfer (4.5) are obtained. We therefore averaged the instantaneous transfer over small intervals of time (table 2). The difficulty in

Ro	$T_{i,S}$	$T_{f,S}$	$T_{i,L}$	$T_{f,L}$	Intervals
0.01	3	6.33	0.47	1.01	$I_{\binom{S}{L}}1$
0.2	3	7.05	0.48	1.10	$I_{\binom{S}{L}}1$
100	2.88	8.1	0.47	1.27	$I_{\binom{S}{L}}1$
0.01	4.73	8.55	0.75	1.35	$I_{\binom{S}{L}}2$
0.2	5	10.14	0.75	1.35	$I_{\binom{S}{L}}2$
100	5.13	14.25	0.8	2.16	$I_{\binom{S}{L}}2$
0.01	7.1	11.41	1.12	1.8	$I_{\binom{S}{L}}3$
0.2	8	14.6	1.25	2.23	$I_{\binom{S}{L}}3$
100	9.9	27.2	1.52	4.01	$I_{\binom{S}{L}}3$
0.01	10.5	15.5	1.65	2.43	$I_{\binom{S}{L}}4$
0.2	13.2	21.64	2.01	3.3	$I_{\binom{S}{L}}4$
100	22.22	58.4	3.3	8.5	$I_{\binom{S}{L}}4$

TABLE 2. Calculated time intervals for each resolution and Ro such that: $I_{\binom{S}{L}}1$, $I_{\binom{S}{L}}2$, $I_{\binom{S}{L}}3$ and $I_{\binom{S}{L}}4$ start at the 10th, 20th, 35th and 50th eddy-turnover time for both the small and the large box, S and L respectively. All intervals are about $N_{t_i,t_f} \approx 20$ eddy-turnover times in length.

choosing the right way to average such quantities temporally is first due to our choice not to force the dynamics. Second, a wide range of rotation rates were investigated, implying a large diversity in the dynamical time scales of the turbulence. Finally, we aim to study the influence of the domain size on the turbulence. All these factors lead to the need for careful consideration of the best choice of time intervals on which to average in order to ensure a comparison of results that are dynamically consistent. In order to estimate the dynamical time scale for each rotation rate and resolution, we used a different definition of the eddy turnover time that has proven useful in decaying simulations. Following Bartello & Warn (1996)

$$N_{t_i,t_f} = \int_{t_i}^{t_f} V(t')^{1/2}\,\mathrm{d}t', \tag{4.6}$$

where N_{t_i,t_f} is the number of eddy turnover times, $V = \frac{1}{2}\int\int\int |\boldsymbol{\omega}|^2\,\mathrm{d}v$ is the enstrophy and t_i, t_f are initial and final times of integration, respectively. The selected time averaging protocol uses N as our measure of the dynamical time for each Ro and for each of the grids. Starting from that point we constructed several time intervals of approximately 20 eddy turnover times (calculated using N_{t_i,t_f} and given in table 2 for three Ro as examples). We integrated $\mathscr{T}_{23}(t;Ro)$ on each of these intervals. The transfers

$$T_{23}(Ro) = \int_{I\binom{S}{L}i} \mathscr{T}_{23}(t;Ro)\,\mathrm{d}t \;= \int_{I\binom{S}{L}i}\int T_{2\_33}(\boldsymbol{k}\in V_{\boldsymbol{k}},t;Ro)\,\mathrm{d}^3\boldsymbol{k}\,\mathrm{d}t \tag{4.7}$$

are shown in figure 6 for time intervals $i = 1$, 2, 3 and 4 as a function of Ro. $Ro\to\infty$ was replaced by $Ro = 10^3$ to fit in figure 6. Linear and logarithmically spaced time intervals gave similar results. Nevertheless, the intervals described above and used in figure 6 allow a better comparison between the small and large domains.

The result is a systematic peak of T_{23} centred around the same Rossby numbers for both computational domains. In addition, the Rossby number of maximum two-dimensional–three-dimensional transfer shows the same systematic translation to

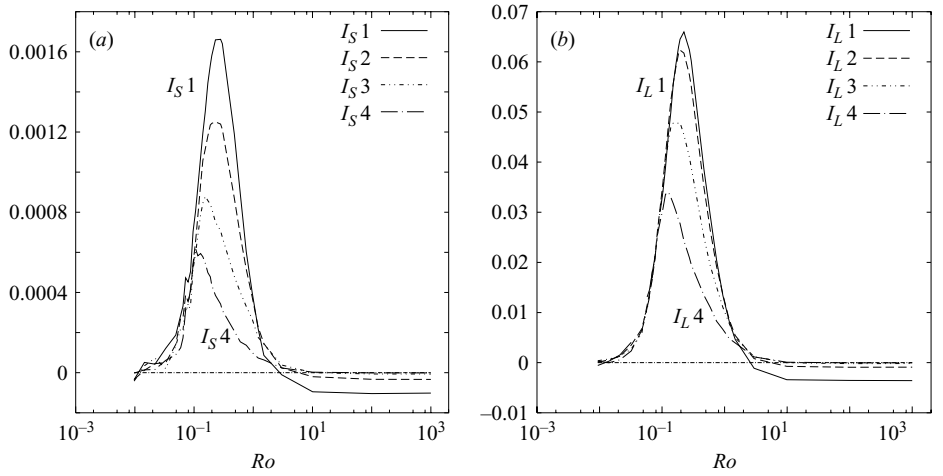

FIGURE 6. Integrated transfer spectra T_{23} using four time intervals of about 20 eddy turnover times (4.6). We start the time intervals $I_{\binom{S}{L}}1$, $I_{\binom{S}{L}}2$, $I_{\binom{S}{L}}3$ and $I_{\binom{S}{L}}, 4$ at about 10, 21, 34 and 50 eddy turnover time scales, respectively. The small (S) domain is presented in (*a*) and the large domain (L) in (*b*).

lower Ro with time for both domain sizes. This translation is due to the decrease of Ro with time in all of our decaying simulations. We conclude that the shape of the curves is robust.

In figure 6, we display the integrated transfer T_{23} as a function of the Ro defined in (3.1). Table 1 gives the equivalent *macro-Ro* for each domain size. From table 1 we can check that doubling the size of the computational domain did not change the values of the *macro-Ro*. We conclude that the use of either (3.1) or the *macro-Ro* definition does not affect the shape of the curves given in figure 6. In other words, both the small and the large box $T_{23}(Ro)$ curves peak around the same value of Ro and evolve similarly regardless of which of our two definitions of Ro is used. The peaks are at $Ro \approx 0.2$, $Ro_{MS} \approx 0.17$ and $Ro_{ML} \approx 0.16$, where Ro_{MS} and Ro_{ML} are the *macro-Ro* of the small and large domains, respectively.

For rotations weaker than $Ro \approx 1$, energy transfers are similar to the non-rotating two-dimensional–three-dimensional transfer, where such a decomposition is irrelevant. In fact, it is due to a balance of energy transfer from two-dimensional to three-dimensional modes with that from three-dimensional to two-dimensional modes. Both grids show this large-Ro behaviour, at all times. One might expect these turbulent statistics to be monotonic with rotation but figure 6 shows that this is clearly not the case. In fact, the peak of energy transfer is reached around $Ro \approx 0.2$ at early times and is robust to the change of domain size. The sign of this transfer is positive, implying an energy flow from wave to vortical energy. This intermediate range is observable between $Ro \approx 0.03$ and $Ro \approx 1$. We refer to the third region, for which Ro is less than approximately 0.03, as the small-Ro range. In this last regime, the integrated transfer T_{23} between waves and vortices is considerably reduced. The increase of the numerical box size reduces the variability on the low-Ro side. The amplitude of the T_{23} peak for the small box decreases faster than that of the large box. This is probably due to the differing dissipation ranges. The low-Ro wing of the peak seems to be time invariant, unlike the high-Ro wing. Again, this property is independent of domain size. Because of the similar behaviour in both domain sizes, we conclude that the peak's centre is not shifted by a change of the numerical sampling of near-resonant interactions

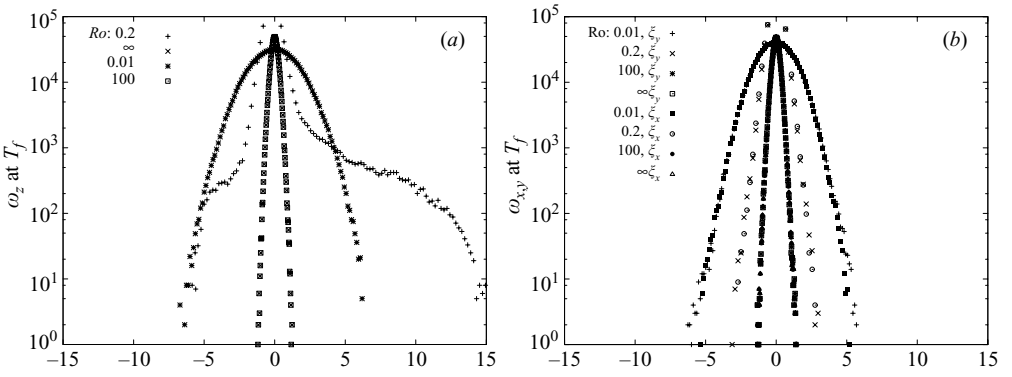

FIGURE 7. Histogram of the three components of the vorticity vector for different Ro at the final time of the simulation T_f. (*a*) The vertical vorticity component ω_z and (*b*) (x, y) components $\omega_{x,y}$. The histograms are shown for the small box. The strongest skewness of the intermediate zone is observed for $Ro = 0.2$.

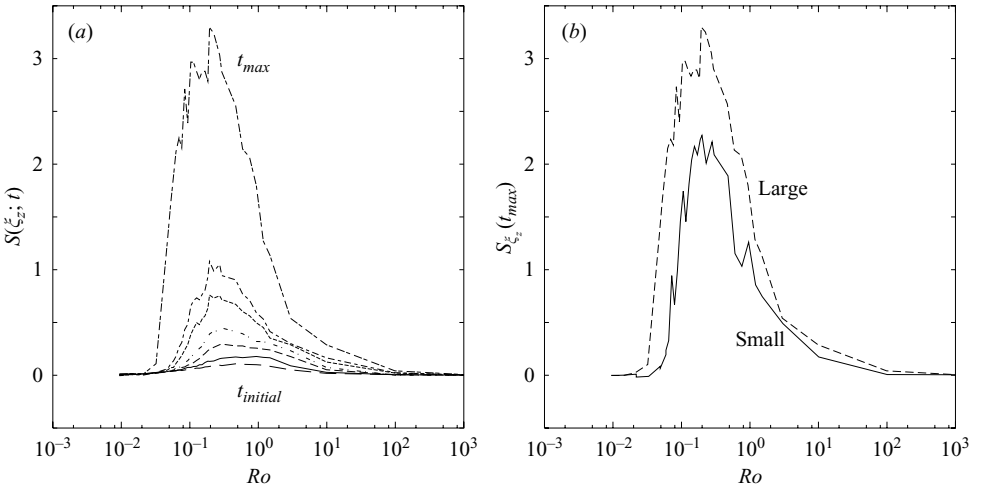

FIGURE 8. (*a*) Skewness of the vorticity component $S(\omega_z)$ as a function of Ro in the large-box simulation, at 7 times (seven). The largest skewness is observed at the last output time, $t_{max,large} = 8.5$. (*b*) The value of $S(\omega_z)$ at the end of the simulations are displayed with Ro, for both the small and large boxes, respectively (i.e. at times $t_{max,small} = 27$ and $t_{max,large} = 8.5$).

nor by the change in sampling of discrete Fourier modes and the subsequent angular resolution in $\boldsymbol{k}$.

4.2. *Skewness*

The skewness of the vertical component of the vorticity $S(\omega_z)$ shows a maximum growth in the intermediate-Ro range for both domain sizes (the histogram for the small-box run is shown in figure 7(*a*)). Horizontal components of vorticity never show this asymmetry, independently of Ro and the size of the computational box (figure 7(*b*)). The growth of the skewness with time in figure 8(*a*) is particularly strong for the intermediate-Ro zone. We observe that its maximum is reached toward the end of the simulations. The maximum skewness value occurs for $Ro \approx 0.2$. These last two results are observable in figure 8(*a*) for the large box. We then compare the

$S(\omega_z) = f(Ro)$ curves for both domain sizes. We chose to display $S_{small}(\omega_z)(t_{max}; Ro)$ and $S_{large}(\omega_z)(t_{max}; Ro)$ in figure 8(*b*), where t_{max} is the time at which $S(\omega_z)$ is a maximum, which occurs at the end of the simulation. Both curves displayed in figure 8(*b*) show a maximum skewness for $Ro \approx 0.2$. This strong asymmetry in favour of cyclonic vortices coincides with a strong energy transfer from waves to two-dimensional modes. Finally, the left wing of the histogram in figure 7 seems Gaussian, which might suggest a reduction of energy transfer for anticyclonic vorticity, as noted by Bartello *et al.*(1994).

Real-space horizontal slices (x, y) of the two-dimensional vertical vorticity field $\omega_{z,2D}$ and vertical slices (y, z) of the total vertical vorticity field ω_z are shown in figure 9 for $Ro = 100$, 0.2 and 0.01. A strongest skewness is observed in the horizontal slices of the two-dimensional vertical vorticity field for $Ro = 0.2$, in which the highest value of vorticity is 100, while the lowest value is -40. This suggests that a transfer of energy from three dimensions is either preferentially toward cyclonic vortices or that a destabilization of the anticyclones occurs as they are formed (or fed energy). This instability may be similar to that observed in channel or free shear rotating flows mentioned in § 1. The $Ro = 0.2$ vertical slice of $\boldsymbol{\omega}_z$ is dominated by $\boldsymbol{\omega}_{z,2D}$. On the other hand, $Ro = 100$ and 0.01 vertical slices are dominated by the the three-dimensional wave vorticity. At $Ro = 0.01$ a slight asymmetry in the cyclone/anticyclone distribution persists, but the intensity of the vortices, from -10 to 15, is weaker than that observed in the two-dimensional horizontal field at $Ro = 0.2$. Finally, the simulations of the weak rotation regime with $Ro = 100$ are similar to those observed for isotropic non-rotating flows: no significant asymmetry is seen, the intensity of the vortices is reduced with time and no anisotropy is noted.

In the present section we identified three distinct rotation ranges. Among these, the intermediate-Ro range is characterized by a strong three-dimensional to two-dimensional transfer. We illustrated that our main result was robust to the doubling of the domain size, thus confirming the adequate sampling of near-resonances. Moreover, we showed that the maximum three-dimensional to two-dimensional transfer is associated with the maximum vertical vorticity skewness, both reached in the intermediate-Ro range for $Ro \approx 0.2$. This is also robust to the change of computational domain size. We examine the three rotating regimes further in the following section § 4.3.

4.3. *Large-, intermediate- and small-Ro regimes*

In figure 10 we display horizontal energy spectra of E_{2D}, E_w and E_{3D} and vertical spectra of three-dimensional energy, E_{3D}, for three characteristic Ro values. The vertical spectra $E_{3D}(k_z)$ displayed for all Ro were offset for clarity. Spectra are averaged over two time intervals $t \in [1, 2]$ and $t \in [7, 10]$ of the large-box simulations. As in figure 3, the three values of Ro chosen are 100, 0.2 and 0.01. Figure 11 shows the energy transfer spectra for the simulation in the intermediate range only. The displayed quantities were introduced in (2.14). For consistency, we used the same time-averaging intervals as those used in figure 10. The transfers shown in the left-hand column are averaged at an early stage of the simulation, namely $t \in [1, 2]$. The right-hand column shows transfers that were averaged later in the simulation on $t \in [7, 10]$. Panel (*a*) displays both $T_{2\_22}(k_h)$ and $T_{2\_33}(k_h)$ spectra as they appear in the $E_{2D}(k_h, t)$ equation (2.14). Panel (*b*) shows horizontal transfer spectra that appear in the $E_{3D}(k_h, t)$ equation (2.14). The $T_{2\_33}(k_h, t)$ curves have been added to these graphs for comparison purposes. Finally, panel (*c*) shows the vertical energy transfer spectra of equation (2.14) for $E_{3D}(k_z, t)$.

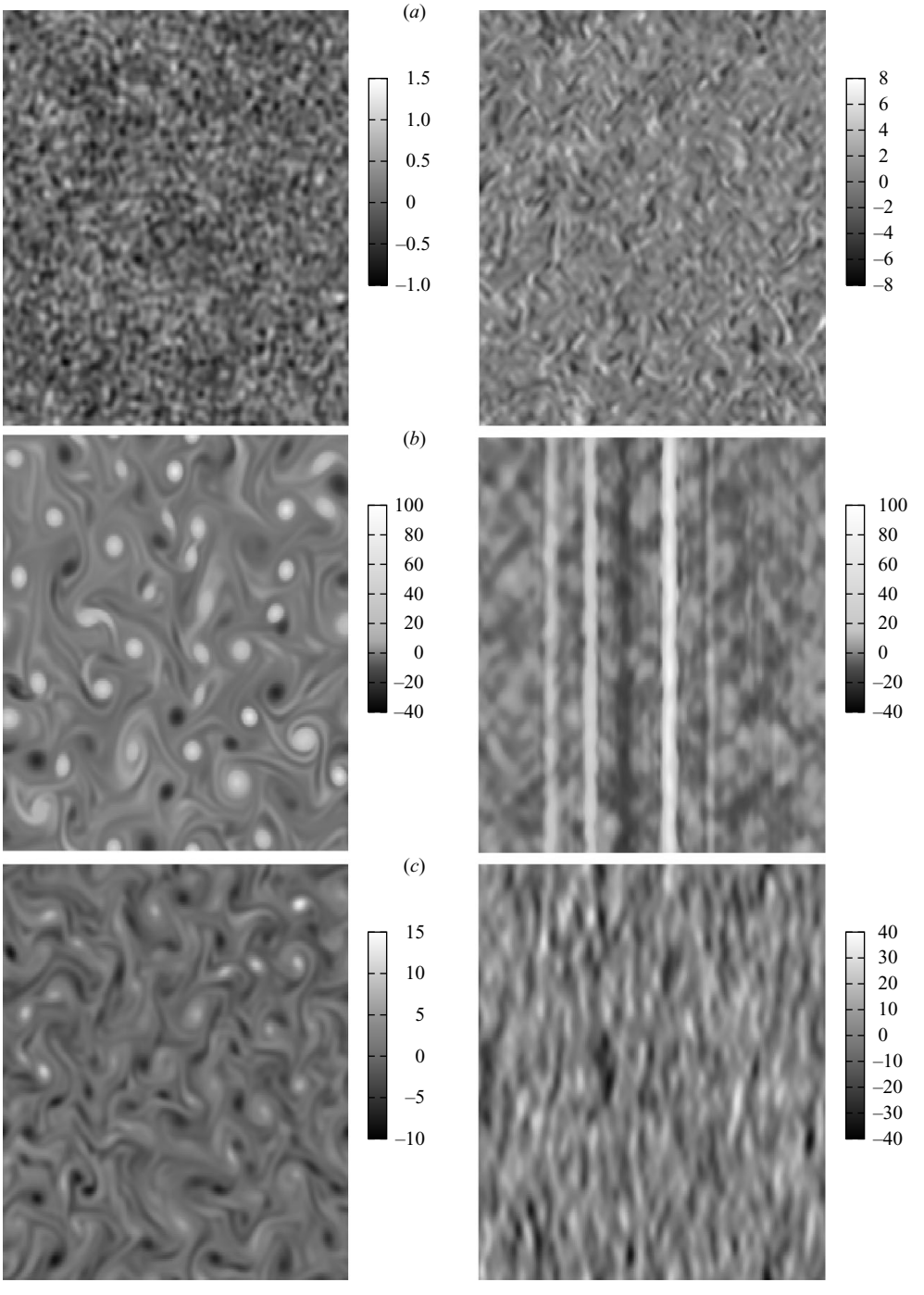

FIGURE 9. Horizontal slices (x, y) of the two-dimensional vertical vorticity field $\omega_{z,2D}$ (left column) and vertical slices (y, z) (right column) of the total vertical vorticity field ω_z for (*a*) $Ro = 100$, (b) $Ro = 0.2$ and (c) $Ro = 0.01$. The snapshots are taken at $t = 8.5$ and from the large-domain simulations.

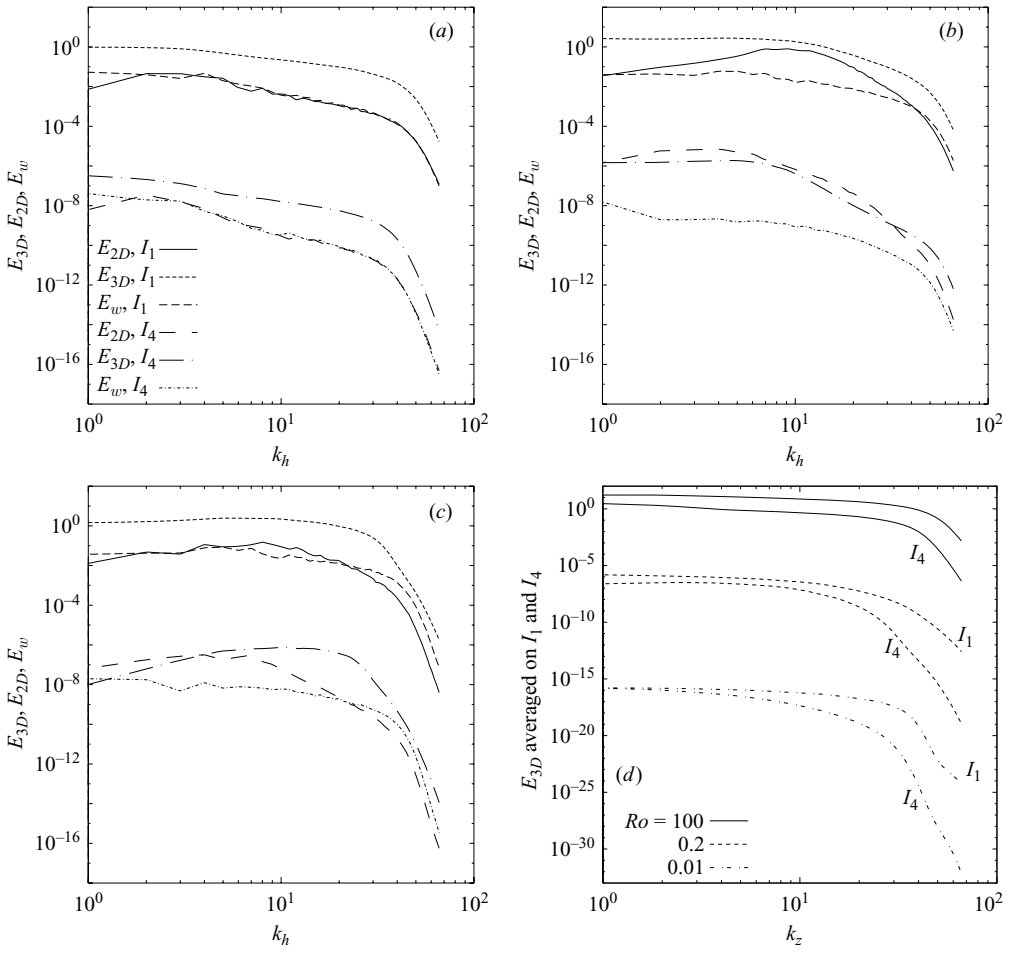

FIGURE 10. The large-box simulations' horizontal spectra of E_{2D}, E_{3D} and E_w averaged on $I_1 = [1, 2]$ and $I_4 = [7, 10]$ time intervals. The spectra averaged on I_1 have been translated upward for clarity. Vertical spectra are displayed for each of (*a*) $Ro = 0.01$, (*b*) 0.2, (*c*) 100 simulations and have been rescaled for clarity. (*d*) The vertical spectra of E_{3D} averaged on I_1 and I_4 are also shown. The small box spectra are similar and are therefore not shown.

From the vertical spectra $E_{3D}(k_z)$ of figure 10, we can see that the vertical transfers are weaker overall than the horizontal for the three Ro and for all times.

The horizontal spectra in figures 10 and 11 of the intermediate-Ro regime show an increase of the two-dimensional energy spectra around $k_h = 10$ early in the simulations. This maximum is due to a preferential transfer from wave modes $k_h \approx 20$ to vortical modes $k_h \approx 10$. Later, these interactions involve a wider range of horizontal wavenumbers. However, the vortical modes that are involved in the injection of two-dimensional energy by the three-dimensional modes remain relatively localized around $k_h = 10$. Later in the simulation, the E_{2D} energy spectrum averaged on $t \in [7, 10]$ shows a migration of its maximum toward larger horizontal scales and a slope $E_{2D}(k_h)/E \sim k_h^{-2.1}$. This is due to the triple-vortex interactions (see $T_{2\_22}(k_h)$) transferring the two-dimensional energy from the injection wavenumber $k_h \approx 10$ to larger horizontal scales (figure 11*a*). Later we still observe this upscale transfer of vortical energy in the $T_{2\_22}(k_h)$ spectrum (figure 11*a*, right).

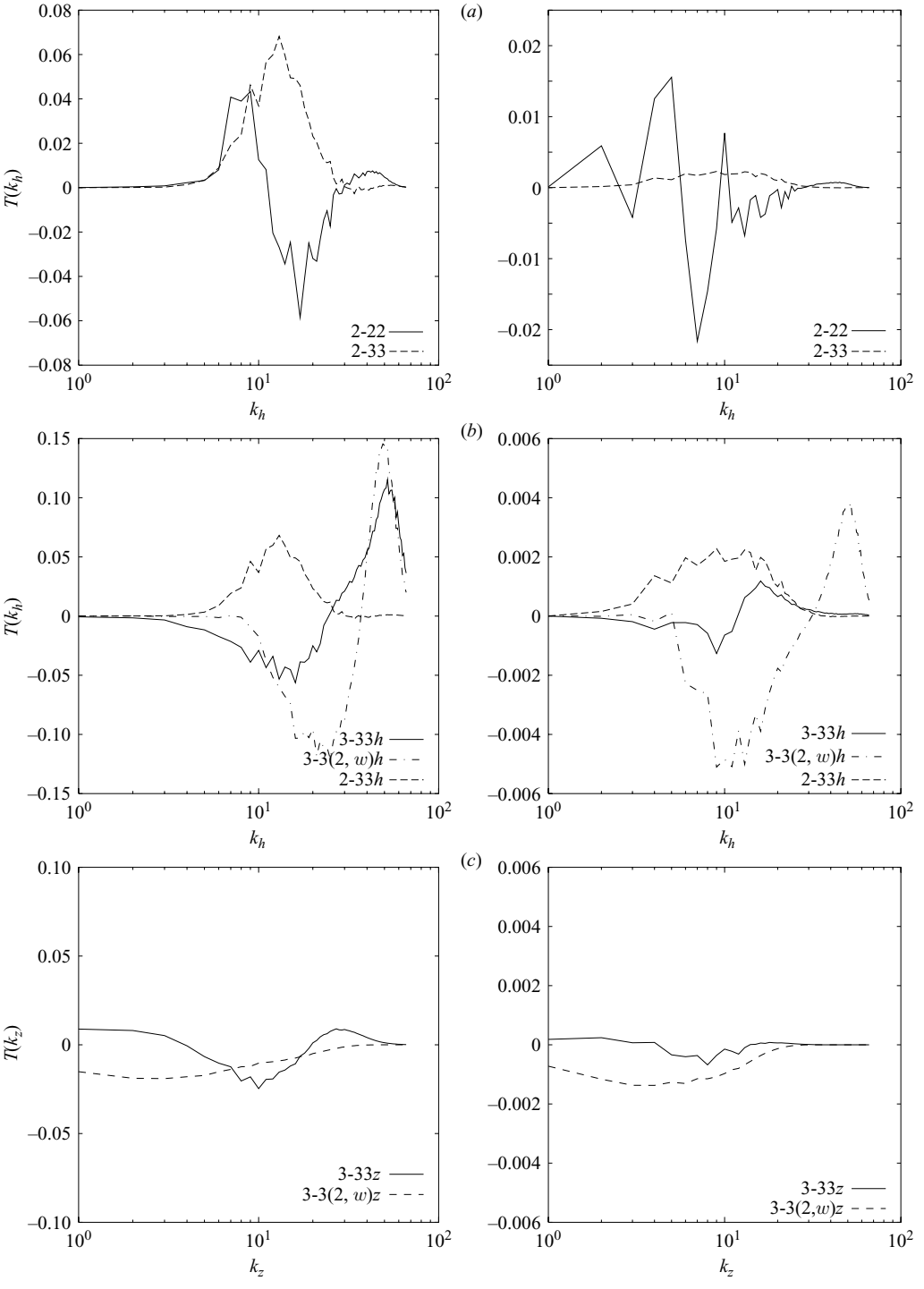

FIGURE 11. Transfer spectra for $Ro = 0.2$ for time intervals $I_1 = [1, 2]$ (left column) and $I_4 = [7, 10]$ (right column).

Over the $Ro = 0.2$ simulation, the E_{3D} is transferred to small horizontal scales via 3-33 and 3-2(w)3 interactions. The associated spectrum gives $E_{3D}(k_h)/E \approx k_h^{-4}$. The decrease of three-dimensional energy with time in favour of the increase of two-dimensional energy leads to a dominant contribution of the $T_{3\_2(w)3}$ with time. These 3-2(w)3 interactions appear to transfer E_{3D} downscale horizontally, but vertically upscale and toward the two-dimensional modes. Unlike the horizontal scale, there is no preferential vertical scale from which energy is extracted to be injected in the $k_z = 0$ modes. The overall amplitudes of the 3-33 vertical transfers ($T_{3\_33}(k_z)$) become smaller than those of the 3-2(w)3 ($T_{3\_2(w)3}(k_z)$) with time. This explains the overall flatness of the vertical spectra $E_{3D}(k_z)$. From both energy and transfer spectra in the intermediate range we conclude that the 3-2(w)3 interactions play the main role in the transfer of three-dimensional energy to dissipation. This transfer is stronger in the horizontal. They also extract three-dimensional energy from all vertical wave scales but from a range of preferred horizontal scales. This extracted energy is preferentially injected in horizontal two-dimensional scales $k_h \approx 10$. In figure 11, the $Ro = 0.2$ energy transfer spectra of $E_w(k_h)$ display a downscale cascade to dissipation scales (not shown). Thus, E_w is systematically dissipated, as observed in figures 4 and 5.

For $Ro = 0.01$, we do not observe a maximum for $E_{2D}(k_h)$ early in the simulation but a maximum of the two-dimensional energy spectrum is noticeable for the second time interval $t \in [7, 10]$ at low wavenumbers. This suggests a migration of two-dimensional energy to larger horizontal scales, but the behaviour is distinct from that observed at $Ro = 0.2$. In fact, the $E_{3D}(k_h)$ spectrum shows a decrease of energy in time for low k_h and a very steep slope between $k_h \approx 20$ and the dissipation range. A comparison of the final values of the $E_{2D}(k_h)$ spectra show that more two-dimensional energy is contained in large horizontal scales for $Ro \approx 0.2$ than for $Ro \approx 0.01$, thus underlining again the distinction between the small- and the intermediate-Ro regimes. The latter shows a stronger two-dimensional upscale energy transfer.

For reference purposes, we provide the large-Ro-regime spectra for $Ro = 100$. In fact, no increase of two-dimensional energy is observed with time for any particular wavenumber, nor is there a sign of two-dimensional energy cascade toward small k_h.

Finally, note that low-rotation-rate simulations have been examined in previous studies and their characteristics are similar to those of isotropic turbulence. We therefore chose not to include them in the spectra discussion. Our examination of transfer spectra of the small-Ro range, such as those at $Ro = 0.01$, is very difficult owing to the significant phase scrambling associated with such high-frequency waves. Ensemble-averaged spectra are necessary to determine how two-dimensional–three-dimensional catalytic resonant interactions compare to those of triple-wave resonant interactions. We do not cover this additional work in the present paper since we chose to focus on what we identified as the intermediate-Ro range.

4.4. *Discussion of the intermediate regime*

Coming back to the vertical transfers and spectra, the overall weakening of vertical transfers observed in § 4.3 is reminiscent of the vertical freezing of energy transfer described by Babin *et al.*(1996) in the limit $Ro \to 0$ (discussed in § 2). Their result is based on the assumption of decoupling in the form of vanishing wave–vortex interactions. However, the $Ro \approx 0.2$ and the intermediate-Ro range in general is characterized by a maximum transfer of energy from wave to two-dimensional modes. Therefore, these two dynamics are different. Moreover, the freezing of vertical energy transfer in Babin *et al.*(1996) is based on their prediction of the dominance of catalytic

resonant wave–vortex interactions over resonant triple-wave interactions in (2.15). It is nevertheless interesting to notice that the intermediate-Ro range shows a dominance of wave–vortex (3-2(w)3) energy transfer over the energy transfer due to triple-wave (3-33) interactions, both horizontally and vertically. So, from this observation one could apply a similar reasoning to that applied to resonant interactions by Babin *et al.*(1996). This could explain the overall reduction of vertical energy transfers compared to those in the horizontal in the intermediate-Ro range. This assumes that 3-2(w)3 transfers dominate 3-33 transfers.

The upscale energy transfer observed in the forced simulations of Smith & Waleffe (1999) and the higher Ro examined by Chen *et al.*(2005) are consistent with the energy transfer in the intermediate simulations range (e.g. $Ro \approx 0.2$) of our decay simulations. The growth of the mean energy-containing scale that is observed in § 4.3 is weaker than that of the forced simulations of Smith & Waleffe (1999) and Chen *et al.*(2005). This is possibly due to the lack of forcing. Moreover, we initialized our rotating simulations with an isotropic spectrum not strongly peaked at a particular wavenumber.

Based on our results in § 4.1, the intermediate-Ro regime is also associated with a strong vorticity asymmetry in favour of cyclones. This last characteristic is also in agreement with Smith & Lee (2005) and shows that the results discussed in Smith & Waleffe (1999), Chen *et al.*(2005) (the highest of the two Ro simulations) and Smith & Lee (2005) all belong to the intermediate-Ro range that we identified above. This, combined with § 4.3, suggests that the lower of the two Ro simulations discussed in Chen *et al.*(2005) belongs to the small-Ro range. The regime separation that we observe should also be evident in forced simulations. Clearly, an investigation in that configuration is needed.

5. Conclusions

We have examined the general picture of rotating turbulence for a large range of Ro (32 values were used). We observe a non-monotonic tendency as $Ro \to 0$. Moreover, we identify three distinct rotation ranges: the large ($Ro > 1$), the intermediate ($0.03 < Ro < 1$) and the small ($Ro < 0.03$). This identification is robust to a doubling of the computational domain size and is therefore not due to poor sampling of the key wave–vortex near-resonant interactions. It is also robust to whether a velocity- or a vorticity-based Rossby number is employed. We show that the intermediate-Ro range is characterized by a maximum leakage of energy from three-dimensional to two-dimensional modes that is initially reached at $Ro \approx 0.2$ for both domain sizes. This transfer is associated with a maximum of vertical vorticity skewness, also reached at $Ro \approx 0.2$. This is also robust to the change of domain size. These results lead us to a general picture of rotating turbulence.

It is interesting to note the analogy between the zero-frequency two-dimensional modes in rotating turbulence and the zero-frequency vertically sheared horizontal flow modes in stratified turbulence. Such an analogy has been mentioned by Smith & Waleffe (2002) concerning the accumulation of zero-frequency energy in either rotating or stratified cases. Moreover, Smith & Waleffe (2002) observed a pile-up of energy in shear modes in their forced numerical simulations. In their forced simulations, Waite & Bartello (2004) observed a similar significant increase of shear-mode energy as the horizontal Froude number decreased down to a threshold value, followed by a significant drop as stratification increased. This last non-monotonic tendency is reminiscent of the non-monotonic behaviour of the intermediate-Ro range in our

rotating decaying simulations. A more systematic study of the stratified case would be necessary to push this analogy further.

The wave–vortex interactions responsible for the intermediate-Ro range preferentially inject wave energy to intermediate-to-small horizontal zero-frequency mode scales ($k_h \approx 10$). They extract three-dimensional energy from all vertical wave scales but preferentially from rather localized intermediate-to-small horizontal scales. Most of the resulting two-dimensional energy is contained in cyclonic vortices of medium horizontal scale. The contribution of triple-wave interactions to the three-dimensional energy transfer is weaker in this regime. Triple-wave interactions have a weaker contribution in vertical energy transfers that are mostly done by wave–vortex interactions.

Finally, the intermediate-Ro range shows a stronger two-dimensional upscale energy transfer than that observed in the small-Ro range. In fact, we could broadly say that the two-dimensional turbulence of the intermediate-Ro range is forced by an injection of energy from wave modes, thus a stronger growth of the two-dimensional energy-containing scale is observed. On the other hand, the integrated transfer, energy spectra and energy time series of the small-Ro range show a vanishing conversion of wave to vortex energy. This is consistent with the vortical dynamics being quasi-independent from the background wave turbulence, but a further computationally demanding study of this last range is necessary for a more complete investigation of the theories discussed in § 1.

We would both like to acknowledge financial support from the Natural Sciences and Engineering Research Council. We would like to thank C. Cambon, K. Ngan, K. Spyksma and M. Waite and acknowledge the Consortium Laval-UQAM-McGill et l'Est du Québec (CLUMEQ) supercomputer centre.

REFERENCES

Asselin, R. 1972 Frequency filter for time integrations. *Mon. Weath. Rev.* **100**, 487–490.

Babin, A., Mahalov, A. & Nicolaenko, B. 1996 Global splitting, integrability and regularity of 3D Euler and Navier-Stokes equations for uniformly rotating fluids. *Eur. J. Mech. B/Fluids* **15**, 291–300.

Babin, A., Mahalov, A. & Nicolaenko, B. 1998 On nonlinear baroclinic waves and adjustment of pancake dynamics. *Theor. Comput. Fluid Dyn.* **11**, 215–256.

Bardina, J., Ferziger, J. H. & Rogallo, R. S. 1985 Effect of rotation on isotropic turbulence: computation and modelling. *J. Fluid Mech.* **154**, 321–336.

Baroud, C. N., Plapp, B. B., She, Z.-S. & Swinney, H. L. 2002 Anomalous Self-Similarity in a Turbulent Rapidly Rotating Fluid. *Phys. Rev. Lett.* **88**, 114501-1–4

Bartello, P., Métais, O. & Lesieur, M. 1994 Coherent structures in rotating three-dimensional turbulence. *J. Fluid Mech.* **273**, 1–29.

Bartello, P. & Warn, T. 1996 Self-similarity of decaying two-dimensional turbulence. *J. Fluid Mech.* **326**, 357–372.

Bellet, F., Godeferd, F. S., Scott, J. F. & Cambon, C. 2006 Wave-turbulence in rapidly rotating flows. *J. Fluid Mech.* **562**, 83–121.

Benney, D. J. & Newell, A. C. 1969 Random wave closure. *Stud. Appl. Math.* **48**, 29–53.

Benney, D. J. & Saffman, P. G. 1966 Nonlinear interaction of random waves in a dispersive medium. *Proc. R. Soc. Lond.* A **289**, 301–320.

Bidokhti, A. A. & Tritton, D. J. 1992 The structure of a turbulent free shear layer in a rotating fluid. *J. Fluid Mech.* **241**, 469–502.

Boyd, J. P. 1989 Chebyshev & Fourier Spectral Methods. Springer.

Caillol, P. & Zeitlin, V. 2000 Kinetic equations and stationary energy spectra of weakly nonlinear internal gravity waves. *Dyn. Atmos. Oceans* **32**, 81–112.

Cambon, C. & Jacquin, L. 1989 Spectral approach to non-isotropic turbulence subjected to rotation. *J. Fluid Mech.* **202**, 295–317.

Cambon, C., Mansour, N. N. & Godeferd, F. S. 1997 Energy transfer in rotating turbulence. *J. Fluid Mech.* **337**, 303–332.

Cambon, C., Rubinstein, B. & Godeferd, F. 2004 Advances in Wave-Turbulence: Rapidly rotating flows. *New J. Phys.* **6**, 73–102.

Chen, Q., Chen, S., Eyink, G. L. & Holm, D. D. 2005 Resonant interactions in rotating homogeneous three-dimensional turbulence. *J. Fluid Mech.* **542**, 139–164.

Galtier, S. 2003 A weak inertial wave turbulence theory. *Phys. Rev. E* **68**, 015301(R)-1–4.

Galtier, S., Nazarenko, S., Newell, A. C. & Pouquet, A. 2000 A weak turbulence theory for incompressible MHD. *J. Plasma Phys.* **63**, 447–488.

Greenspan, H. P. 1968 The theory of rotating fluids. Cambridge University Press.

Hopfinger, E. J., Browand, K. F. & Gagne, Y. 1982 Turbulence and waves in a rotating tank. *J. Fluid Mech.* **125**, 505–534.

Jacquin, L., Leuchter, O., Cambon, C. & Mathieu, J. 1990 Homogeneous turbulence in the presence of rotation. *J. Fluid Mech.* **220**, 1–52.

Johnson, J. A. 1963 The stability of shearing motion vertical in a rotating fluid. *J. Fluid Mech.* **17**, 337–352.

McEwan, A. D. 1969 Inertial oscillations in a rotating fluid cylinder. *J. Fluid Mech.* **40**, 603–640.

McEwan, A. D. 1976 Angular momentum diffusion and the initiation of cyclones. *Nature* **260**, 126–128.

Morinishi, Y., Nakabayashi, K. & Ren, S. Q. 2001a Dynamics of anisotropy on decaying homogeneous turbulence subjected to system rotation. *Phys. Fluids* **13**, 2912–2922.

Morize, C., Moisy, F. & Rabaud, M. 2005 Decaying grid-generated turbulence in rotating tank. *Phys. Fluids* **17**, 095105-1–11

Newell, A. 1969 Rossby wave packet interactions. *J. Fluid Mech.* **35**, 255–271

Rothe, P. H. & Johnston, J. P. 1979 Free shear layer behaviour in rotating systems. *Trans. ASME: J. Fluids Engng* **101**, 117–120.

Smith, L. M. & Waleffe, F. 1999 Transfer of energy to two-dimensional large scales in forced, rotating three-d imensional turbulence. *Phys. Fluids* **11**, 1608–1622.

Smith, L. M. & Waleffe, F. 2002 Generation of slow large scales in forced rotating stratified turbulence. *J. Fluid Mech.* **451**, 145–168.

Smith, L. M. & Lee, Y. 2005 On near resonances and symmetry breaking in forced rotating flows at moderate Rossby number. *J. Fluid Mech.* **535**, 111–142.

Tritton, D. J. 1992 Stabilization and destabilization of turbulent shear flow in a rotating Fluid. *J. Fluid Mech.* **241**, 503–523.

Waite, M. L. & Bartello, P. 2004 Stratified turbulence dominated by vortical motion. *J. Fluid Mech.* **517**, 281–308.

Waleffe, F. 1992 The nature of triad interactions in homogeneous turbulence. *Phys. Fluids* A **4**, 350–363.

Waleffe, F. 1993 Inertial transfers in the helical decomposition. *Phys. Fluids* **5**, 677–685.

Witt, H. T. & Joubert, P. N. 1985 Effect of rotation on turbulent wake. *Proc. 5th Symp. on Turbulent Shear Flows, Cornell* 21.25–21.30.

Yeung, P. K. & Zhou, Y. 1998 Numerical study of rotating turbulence with external forcing. *Phys. Fluids* **10**, 2895–2909.